

Multi-color Cavity Metrology

Kiwamu Izumi,¹ Koji Arai,² Bryan Barr,³ Joseph Betzwieser,⁴ Aidan Brooks,² Katrin Dahl,⁵ Suresh Doravari,² Jennifer C. Driggers,² W. Zach Korth,² Haixing Miao,² Jameson Rollins,^{2,*} Stephen Vass,² David Yeaton-Massey,² and Rana X. Adhikari²

¹*Department of Astronomy, Graduate school of science,*

University of Tokyo, Bunkyo-ku, Hongo, Tokyo 113-0033, Japan

²*LIGO Laboratory, California Institute of Technology MS 100-36, Pasadena, CA 91125, USA*

³*SUPA, School of Physics & Astronomy, University of Glasgow, Glasgow, G12 8QQ, Scotland*

⁴*LIGO Livingston Observatory, P.O. Box 940, Livingston, Louisiana 70754-0940, USA*

⁵*Max-Planck-Institut für Gravitationsphysik (Albert-Einstein-Institut) and Leibniz Universität Hannover, Callinstr. 38, 30167 Hannover, Germany*

Long baseline laser interferometers used for gravitational wave detection have proven to be very complicated to control. In order to have sufficient sensitivity to astrophysical gravitational waves, a set of multiple coupled optical cavities comprising the interferometer must be brought into resonance with the laser field. A set of multi-input, multi-output servos then lock these cavities into place via feedback control. This procedure, known as lock acquisition, has proven to be a vexing problem and has reduced greatly the reliability and duty factor of the past generation of laser interferometers. In this article, we describe a technique for bringing the interferometer from an uncontrolled state into resonance by using harmonically related external fields to provide a deterministic hierarchical control. This technique reduces the effect of the external seismic disturbances by four orders of magnitude and promises to greatly enhance the stability and reliability of the current generation of gravitational wave detector. The possibility for using multi-color techniques to overcome current quantum and thermal noise limits is also discussed.

© 2013 Optical Society of America

OCIS codes: 120.3180, 120.2230, 140.3515, 310.6805, 350.1270

1. Introduction

Gravitational waves promise to reveal new information about the bulk motions of massive compact objects in the universe. In this decade kilometer-scale interferometers, such as LIGO [1, 2], Virgo [3], GEO600 [4], and KAGRA [5], are expected to make the first direct detection of gravitational waves in the 10-10k Hz band. The Advanced LIGO (aLIGO) project [6] is a significant upgrade of the initial LIGO interferometers, including more sophisticated vibration isolation, a factor of ten higher laser power, larger test masses, and a more versatile optical readout, among other improvements. These improvements should lead to a factor of 10 sensitivity improvement across the entire detection band, resulting in a factor of 1000 in increased probed volume of space.

The problem of moving an interferometer from its initial uncontrolled state (where the suspended mirrors are swinging freely) to the final operating state (where all cavity lengths are interferometrically controlled) is referred to as “lock acquisition”. For a single Fabry-Perot cavity or a simple Michelson interferometer, the prob-

lem is relatively straightforward: typically the locking servo is engaged and the mirrors are moved until the servo forces the interferometer into the desired operating point. With a more complicated configuration utilizing multiple coupled cavities (e.g. aLIGO) there are no reliable optical signals providing cavity length information until all cavities are simultaneously resonant. This problem is compounded by seismic-induced residual mirror motions which, even with the advanced seismic isolation systems used in aLIGO, are expected to be $\sim 10^{-7}$ m below 1 Hz [7]. Waiting for full acquisition to happen by chance is an exercise in futility.

Over the years various techniques have been developed to address the lock acquisition problem. Algorithms have been developed that use digital controls, clever sequencing of feedback loops and mixing of interferometric signals to reduce the waiting time [8–10]. Unfortunately, these are still insufficient for the needs of aLIGO. Instead, aLIGO will be using an auxiliary arm length stabilization system to robustly bring the long arm cavities to a stable operating point at the cavity resonance, independent of the rest of the interferometer. This technique uses frequency-doubled auxiliary lasers, phase locked to the main interferometer laser source, to serve as an independent sensor for the cavity lengths. The primary motivation of the experiment described in this article is

*Corresponding author: jrollins@ligo.caltech.edu

to demonstrate that the arm cavity length can be independently controlled by auxiliary locking to within a small fraction of the linewidth of the arm cavity at the primary laser frequency.

Beyond the practical application of aLIGO arm length stabilization, this type of “multi-color metrology” can allow us to make better measurements of cavity properties and noise fluctuations. This may one day make it possible to sense inherent noise sources and reduce their metrological effects.

Arm length stabilization with frequency-doubled auxiliary lasers has been demonstrated by Mullavey et. al [11] in shorter-baseline cavities. Other methods for independent arm cavity stabilization have included *digital* interferometry [12, 13], and *suspension point* (or *suspension platform*) interferometry [14, 15].

This article describes a prototype experiment of cavity length stabilization using multiple laser wavelengths, and its implications for future interferometers. The experiment has been performed on a 40-meter-long suspended Fabry-Perot cavity. Possible noise sources and their contributions are discussed.

2. Experimental Setup

This experiment was conducted on the Caltech-LIGO 40m prototype interferometer [16–18]. This prototype is used to develop interferometer topologies for future gravitational wave detectors. Currently the configuration is similar to that of aLIGO (dual-recycled Michelson with 40m-long Fabry-Perot arm cavities), and is being used to prototype aLIGO readout and control schemes. “Dual-recycling” refers to the use of both power and signal recycling mirrors at the input and output ports respectively of the Michelson interferometer, recycling light power that would otherwise escape through those ports [19, 20]. All of the main interferometer optics are suspended as single-stage pendula with a length of 25 cm ($f_p = 1$ Hz). The entire interferometer is housed in an ultra-high vacuum envelope. For this experiment just a single, suspended, 40m-long Fabry-Perot arm cavity of the full interferometer is used. The rest of the interferometer optics are misaligned so as to not affect the measurements.

Figure 1 shows a schematic diagram of the experimental setup. A 1064 nm beam (red in diagram) from the main interferometer pre-stabilized laser (PSL) is injected into the arm cavity through the input mirror (ITM) from the interferometer vertex. A second, 532 nm beam (green in diagram) from an auxiliary (AUX) laser is injected through the cavity end mirror (ETM). Whereas the PSL beam circulates through the full interferometer under normal operating conditions, the AUX laser beam resonates only in the single arm cavity and is extracted before interacting with the rest of the interferometer.

The cavity mirrors are dichroic and highly reflective at both wavelengths. For the 1064 nm beam, the cavity is overcoupled and reflects most of the light back towards the interferometer vertex. For the 532 nm beam

cavity property	symbol	1064 nm	532 nm
ITM power transmissivity	T_i	0.0138	0.0458
ETM power transmissivity	T_e	1.37×10^{-5}	0.0109
power trans. (resonance)	T_c	3.92×10^{-3}	0.616
power trans. (anti-resonance)	T_c^\dagger	4.77×10^{-8}	1.29×10^{-4}
finesse	\mathcal{F}	450	109
cavity pole frequency	f_c	4.40 kHz	18.3 kHz
cavity length	L	37.8 m	
free spectral range	f_{FSR}	3.97 MHz	

Table 1. Cavity properties of the arm cavity, at 1064 nm as seen from the vertex, and 532 nm as seen from cavity end.

the cavity has a much higher transmissivity and some of the light is transmitted through the cavity at the ITM, through the interferometer vertex and extracted from the vacuum. The mirror and cavity properties for both wavelengths are shown in Table 1.

A. PSL light source

The 1064 nm light source is a 2 W Innolight NPRO. The light is spatially filtered by a ~ 20 cm ring cavity with a ~ 2 MHz bandwidth that also provides passive filtering of the laser noise at RF frequencies. The PSL frequency is locked to an in-vacuum, suspended, critically-coupled, triangular mode cleaner (MC) cavity, which conditions the beam by suppressing excess frequency noise and rejecting higher-order spatial modes. The laser is locked to the MC via the standard Pound-Drever-Hall (PDH) method [21] with a ~ 130 kHz bandwidth. The power is adjusted to allow approximately 25 mW of 1064 nm laser light to be incident on the cavity under test.

B. AUX light source and frequency doubling

The AUX beam comes from a frequency-doubled 700 mW JDSU NPRO-126N. The frequency doubling is achieved via second harmonic generation (SHG) in a PPKTP crystal [22]. The conversion efficiency is $\sim 1\%/W$, and with other input losses we end up with 1.2 mW of 532 nm light incident on the ETM.

C. Dichroic mirror coatings

The mirrors forming the Fabry-Perot arm cavities have custom coatings to provide reflectivity at both 1064 and 532 nm. Figure 2 shows the calculated coating reflectivity as a function of wavelength for the ITM (the ETM shows a similar profile). The layer structure is a particular aperiodic design chosen to minimize the influence of various types of thermal noise on the reflected phase of the laser field [23].

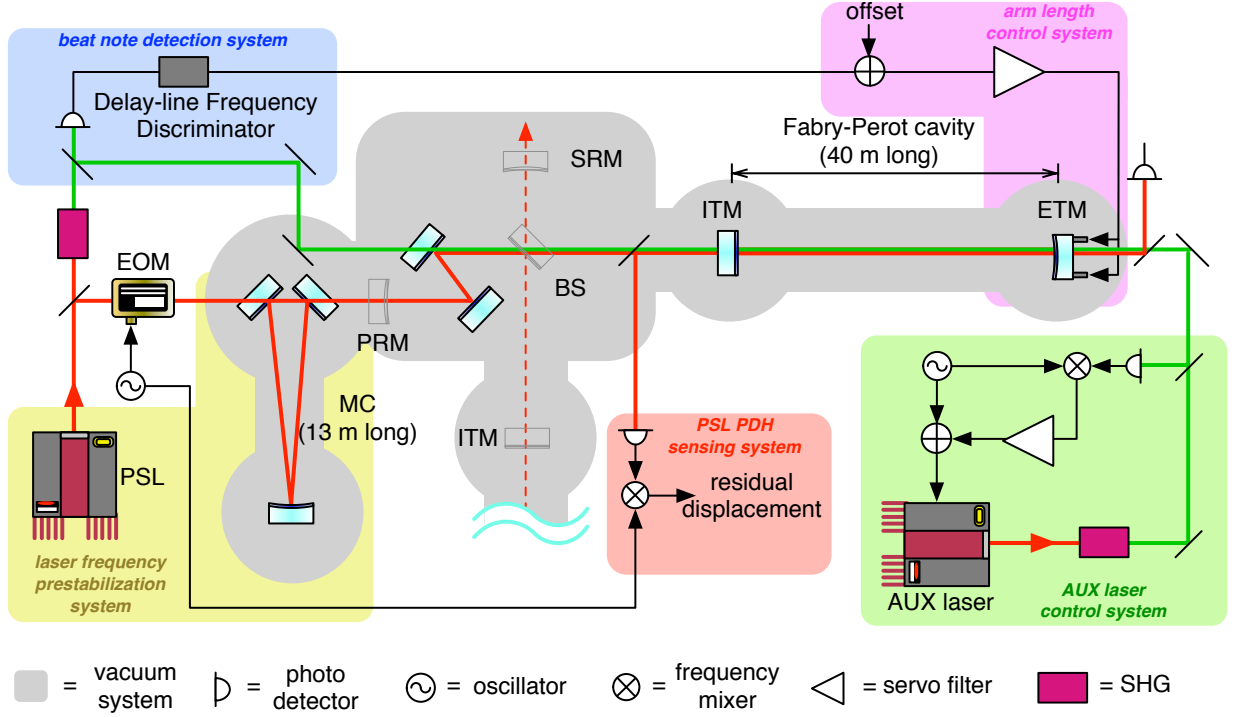


Fig. 1. Experimental setup. Red lines indicate the path of the 1064 nm PSL beam, and green lines indicate the path of the 532 nm AUX beam. The colored regions correspond to logical sections of the control and readout, described in more detail in Section 3. Optics in shadow are part of the larger interferometer not used in this experiment.

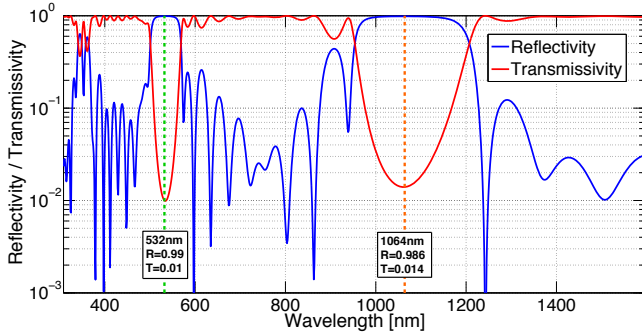


Fig. 2. Spectral reflectivity of one of the dichroic cavity mirrors.

D. Sensing, acquisition and control

Initially, the AUX laser frequency is locked to the arm cavity length via a standard PDH locking scheme. The AUX laser is locked to the cavity, rather than vice versa, because the laser frequency actuator has much greater bandwidth than the cavity mirror displacement actuators. Phase modulation sidebands at 217 kHz are introduced on the AUX beam by directly driving the laser frequency actuator. This modulation frequency is chosen to minimize the ratio of amplitude to phase modulation.

The green light reflected from the ETM is used for the PDH lock.

Once the AUX laser is locked to the cavity, the AUX beam transmits through the ITM and is extracted from the vacuum system. The extracted AUX beam is used in a heterodyne measurement with a frequency-doubled sample of the PSL beam. The frequency of the beat note between the AUX laser and the frequency-doubled PSL is measured by the a delay-line frequency discriminator (DFD) (see section 2E). The DFD has “coarse” and “fine” paths which provide different dynamic ranges. These outputs are the primary error signal for the cavity control. They are digitized and a control signal is generated with a digital feedback control system.

Figure 3 shows the control sequence and hand-off between the coarse and fine discriminator paths. Since seismic noise acting on the length of the MC and arm cavities causes the beat note to fluctuate by about 10 MHz, the large range coarse path is used to engage feedback smoothly. After length control is achieved an artificial offset is introduced in the discriminator signal to sweep the length of the arm cavity until the length meets the resonance condition for the PSL beam. This ability to tune the cavity length directly is the key to the use of this technique as a lock acquisition tool for Advanced LIGO.

In the end, control is passed to the fine discriminator by digitally fading over between the coarse and fine

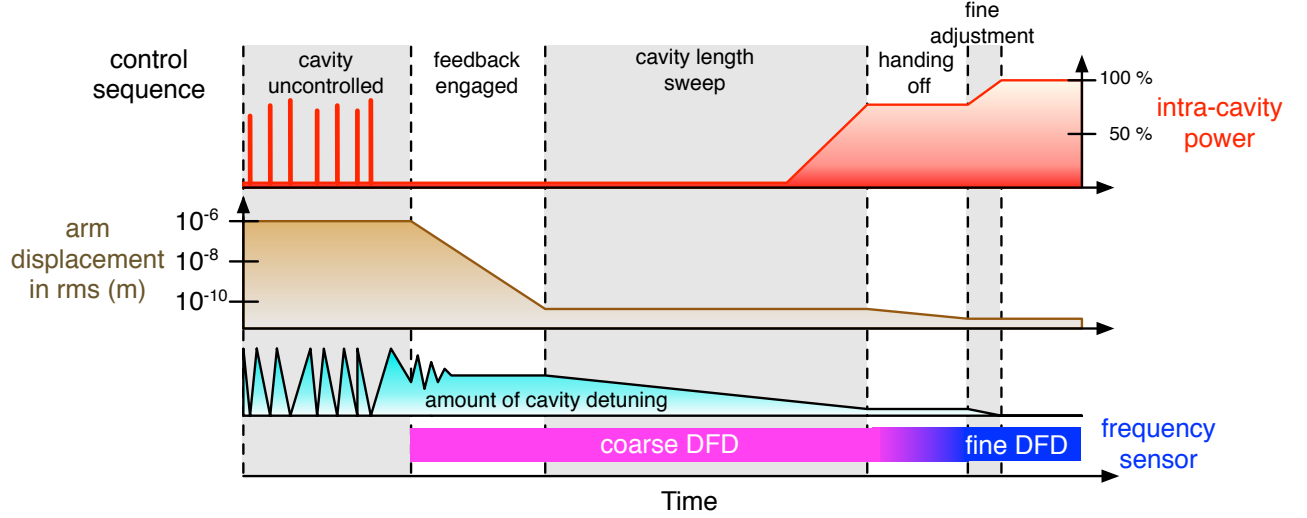


Fig. 3. Sequence of the arm length control as a function of time. The intra-cavity power and detuning are for the 1064 nm PSL beam.

signals. The fine discriminator has a higher signal-to-noise by a factor of the extra delay. At this stage the arm length can be tuned more precisely so that the main laser fully resonates in the arm. The final steady-state control used during the measurement is described in detail in section 3. A PDH error signal derived from the PSL beam reflected off of the ITM provides an out-of-loop measure of the residual cavity displacement.

E. Delay-line frequency discriminator

The delay-line frequency discriminator (DFD), which is used to measure the frequency of the beat note between the PSL and AUX beams, works by mixing an input RF signal with a delayed version of itself. For a given delay in the delay line, D , the mixer output voltage is a periodic function of the input frequency, f . In the small frequency limit ($f \ll 1/D$) the output is directly proportional to the input frequency:

$$V \propto Df. \quad (1)$$

Figure 4 shows a schematic of the DFD circuit. The signal from a broadband RF photodetector first passes through a comparator that turns the signal into a square wave. This helps reduce noise associated with small amplitude fluctuations of the input signal. This signal is amplified and split into two discriminator paths: a *coarse* path with a delay of 7.3 ns and frequency range of 34 MHz, and a *fine* path with a delay of 270 ns and a range of 3.6 MHz. The mixer outputs, with signals given by equation 1, are filtered and digitized and used as error signals for the cavity length control servo. The coarse path, which has a larger bandwidth, is used during lock acquisition, whereas the lower-noise fine path is used to achieve best performance in the steady state.

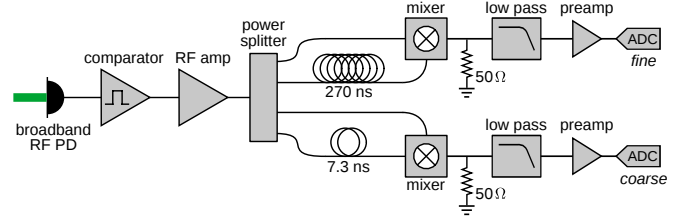


Fig. 4. Delay-line frequency discriminator. Components used: comparator: Analog Devices AD9696; RF amplifier: Mini-Circuits ZHL-1A; power-splitter: Mini-Circuits ZBSC-413+; delay line cables: RG-58 C/U; mixer: Mini-Circuits ZP-3+; low-pass filters: Mini-Circuits BLP-1.9; pre-amplifier: Stanford Research SR560.

In order to confine the cavity length to the within the line width of the PSL a residual fluctuation level of 10 pm RMS must be achieved. This means that the frequency noise of the fine path needs to be less than $7.4 \text{ Hz}/\sqrt{\text{Hz}}$ in the control bandwidth. The noise of the two paths are currently limited by the active readout electronics at an estimated level of $2.0 \text{ Hz}/\sqrt{\text{Hz}}$ and $0.1 \text{ Hz}/\sqrt{\text{Hz}}$ for the coarse and fine paths respectively. They therefore reasonably meet the required frequency stability.

A delay-line design was used, rather than a phase-locked loop (PLL) design [24] because the frequency range of DFDs are relatively easy to tune and can be adjusted to give a large frequency range (e.g. the coarse channel). DFDs also don't require any active feedback loops, which complicate PLLs. Alternatively, a combination of a large range DFD and a smaller range PLL could be a possible solution depending on the required frequency range and noise.

3. Control Model

In this section we present a model of the control system used in the experiment. The control system, shown in Figure 5, can be broken into five parts, each described in the sections below. The model includes injection points for various noise sources that might affect overall performance, discussed in detail in section 4.

A. AUX-cavity loop

The first logical control loop is the PDH lock of the frequency-doubled AUX laser to cavity (green block in Figures 1 and 5). This loop suppresses the frequency noise of the AUX laser and allows its frequency to follow the motion of the cavity length. The control bandwidth of this loop is 30 kHz, limited by the laser cavity PZT frequency actuator.

Since the AUX laser is locked to the cavity, information about the length fluctuation of the cavity is encoded in the frequency of the AUX laser light transmitted through the cavity ITM. The relationship between cavity length and laser frequency is given by:

$$\frac{dL}{L} = \frac{d\nu}{\nu}, \quad (2)$$

where L is the cavity length and ν is the frequency of the laser resonating in the cavity. The cavity frequency response is a function of the cavity finesse and can be approximated as a single-pole low pass filter:

$$C_{\text{AUX}}(f) = \frac{1}{1 + i(f/f_c)}, \quad (3)$$

where f is the frequency of the signal and f_c is the cavity pole frequency, which for the 532 nm AUX beam is 18 kHz.

The photo detection and mixing process that produces the PDH error signal has an overall flat V/Hz conversion factor given by D_{AUX} . The servo filter, which is tuned to provide stable and robust locking, has a frequency response of F_{AUX} . Finally, the laser PZT frequency actuator has a response of A_{AUX} .

The noise sources associated with this loop are the AUX laser frequency noise, second-harmonic generation noise, shot noise at the detector, and electronics noise of the readout electronics. These noise sources will be discussed in detail in section 4.

B. PSL-MC loop

The PSL-MC loop (yellow in Figures 1 and 5) describes the lock of the PSL frequency to the mode cleaner length. The control bandwidth of this loop is 130 kHz. As with the AUX laser cavity loop, the MC cavity has a single-pole frequency response given by C_{PSL} . D_{PSL} is the response of the PDH sensing, F_{PSL} is the response of the servo filter, and A_{PSL} is the response of the PSL compound frequency actuator, which includes the laser crystal temperature actuator, laser cavity PZT, and an EOM phase modulator.

The PSL light transmitted through the MC and incident on the arm cavity under test is the reference for the performance of the cavity stabilization system. However, finite gain in the PSL-MC loop can potentially lead to PSL frequency noise coupling into the arm stabilization loop. Despite this, the model shows that the suppression ratio from PSL frequency noise to residual displacement is more than 10^6 at 100 Hz, so we can safely neglect the PSL frequency noise.

C. Beat note detection

The beat note detection block (blue in Figures 1 and 5) measures the frequency difference between the AUX and frequency-doubled PSL beams.

The transmitted AUX light is a combination of the suppressed AUX laser frequency noise and any external displacement noises in the cavity that modulate the optical phase of the laser resonating in the cavity. These external disturbances result in phase noise that is converted to frequency noise by multiplying by the complex frequency, if . This signal is then low-pass filtered by the cavity pole, C_{AUX} , with a resultant transfer function of:

$$H_{\text{AUX}}(f) = \frac{i(f/f_c)}{1 + i(f/f_c)}, \quad (4)$$

where again $f_c = 18$ kHz. D_{DFD} represents the flat Hz \rightarrow V conversion of the full beat detection process, including the gain of the RF photo detector and the delay-line frequency discriminator.

Noise in the frequency doubling process of the PSL should be at a similar level to that in the AUX-cavity loop. Laser shot and photo-detection noises are also similar to those in AUX-cavity loop. The electronics noise in this case is from the frequency discriminator (DFD). Finally, there is also additional noise from the analog-to-digital conversion (ADC) process.

D. Arm length servo

The output of the beat note detection process is the error signal for the arm cavity length control servo loop (pink in Figures 1 and 5). The digital error signal is sent through the servo filter, F_{ALS} , which includes a 470 μ s processing delay. The resultant digital control signal is converted back to an analog voltage via a digital-to-analog converter (DAC), and the output analog control signal is used to actuate on the end test mass via electromagnetic actuators (A_{TM}). The overall open loop gain of this loop is roughly

$$G_{\text{ALS}} \simeq D_{\text{DFD}} F_{\text{ALS}} A_{\text{TM}}, \quad (5)$$

since the effect of the AUX-cavity loop and H_{AUX} in parallel is an overall flat frequency response that does not affect the overall open-loop gain.

When the loop is closed, fluctuations in the frequency of the beat note are suppressed by acting on the cavity length. Any external disturbances that produce frequency shifts common to both the AUX and PSL beams

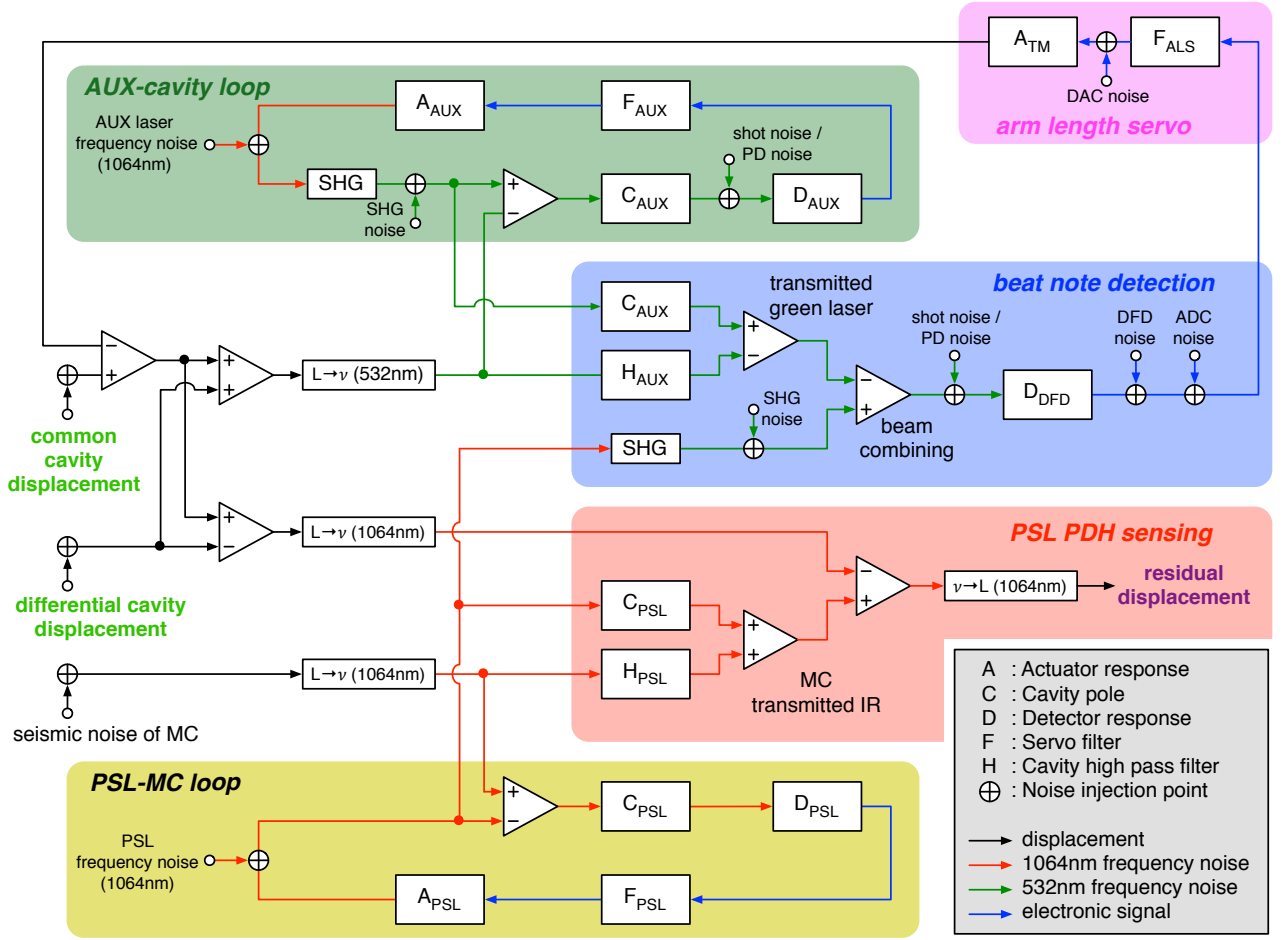


Fig. 5. Block diagram of the model of control scheme and noise sources for the experiment. The colored blocks correspond to the colored blocks in the setup diagram in Figure 1. The various individual control elements are described in the text and in appendix A.

will then be suppressed by the closed loop suppression factor, $1/(1 + G_{ALS})$. The transfer function between disturbances common to both wavelengths and residual displacement can be seen in Figure 8 in appendix A.

E. PSL PDH sensing

This block represents the direct out-of-loop measurement of the residual displacement noise of the cavity relative to the length of the MC. As opposed to the external disturbances common to the AUX and PSL beams that are suppressed by the arm length servo, any external disturbances sensed *differentially* between the AUX and PSL beams will transmit directly to this sensor and contribute to any residual displacement noise. The transfer function between differential external disturbances and residual displacement can be seen in Figure 8 in appendix A.

There are noise sources here related to readout, such as ADC noise, and shot noise and dark noise in the MC transmitted photo detection process, but they are found to be insignificant relative to other noise sources and are therefore omitted.

4. Performance and Noise Analysis

The primary usefulness of the multi-color readout is that it enables us to precisely adjust the arm length and hold it at a desired value independent of the state of the rest of the interferometer (as discussed in section 2). Figure 6 shows a sweep of the cavity length feedback offset through the cavity resonance of the 1064 nm PSL beam. The figure demonstrates that the length detuning can be cleanly and smoothly brought to zero, at which point the 1064 nm beam is fully resonant in the cavity. The top plot is the amount of the detuning in terms of the beat frequency observed at the fine DFD output. The middle plot shows the 1064 nm intracavity power as it passes through resonance with the cavity. The bottom plot shows the PSL PDH error signal.

The residual arm displacement measured in the out-of-loop PSL PDH error signal has a root mean square (RMS) of 23.5 pm, integrated from 1 kHz to 10 mHz. The amplitude spectral density and RMS of this residual displacement are shown as the solid and dashed red

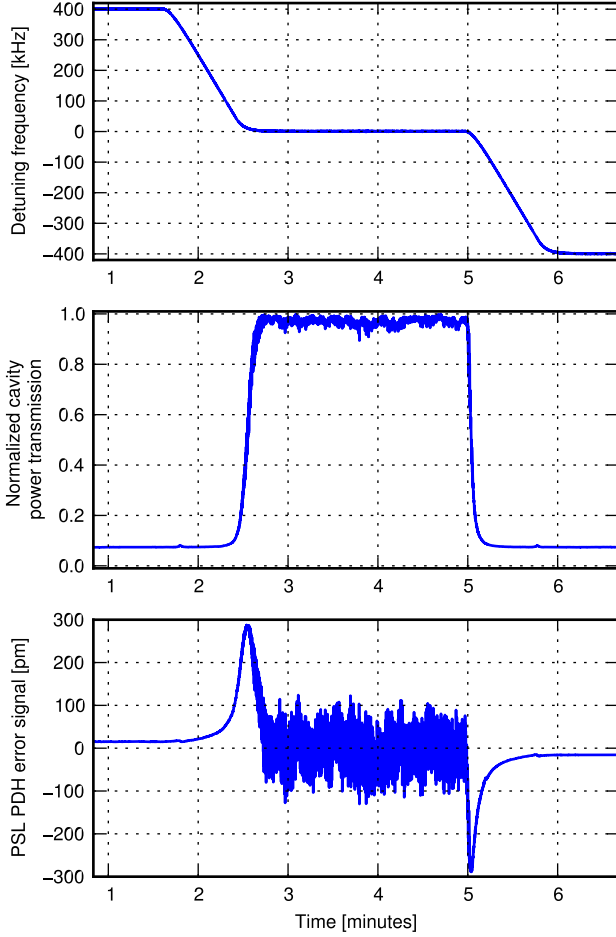


Fig. 6. Sweep of cavity length control offset through the 1064 nm (PSL) resonance of the cavity. A detuning of 100 kHz corresponds to a cavity displacement of 6.7 nm.

curves respectively in Figure 7. The measured RMS falls below the aLIGO requirement of 1.3 nm RMS [25], which is based on the the line width of the arm cavity for the 1064 nm wavelength.

Figure 7 also shows the overall noise budget of the experiment, i.e. an accounting of all noise sources that are thought to affect the performance of the experiment. To determine the contribution from a particular source we first calculate, estimate, or measure the power spectrum of the noise, $S(f)$, at its source (designated by a \oplus in Figure 5), and propagate the amplitude spectrum through the control model to produce an amplitude spectrum in the “residual displacement” output. The result is

$$n(f) = X(f)\sqrt{S(f)}, \quad (6)$$

where $X(f)$ is the transfer function from the noise source to the out-of-loop-measured residual displacement. In the rest of this section we will describe the contribution from each of the sources shown in Figure 7.

The total noise spectrum accountable from the budget is shown as the solid blue trace in Figure 7. The fact

that the blue trace lies below the red trace over much of the band indicates a discrepancy in the noise accounting. The measured displacement spectrum is limited by a $1/f$ -shaped noise at low frequencies, and a white noise above 100 Hz. It is unknown at this time where these limiting factors originate.

Table 3 in Appendix B describes all of the fundamental constants, experimental values, and material properties used in this section.

A. Fundamental cavity noise sources

This section describes various fundamental noise sources in the cavity being measured. While most of these noises can’t be measured directly, their levels can be estimated based on analytical models of the underlying physics.

1. Seismic noise

Seismic noise, while dominant across much of the band of interest, is suppressed by the cavity length control loop. The light gray “unsuppressed” spectrum in Figure 7 is an estimate of the free-swinging cavity motion, $\sqrt{S_{\text{seis}}}$, based on the in-loop error signal when the cavity is locked to the PSL. This spectrum is expected to be entirely dominated by seismic noise at frequencies below 100 Hz, and reaches a level of roughly 10^{-7} m/ $\sqrt{\text{Hz}}$ below 1 Hz. The peak at 1 Hz is due to the pendulum resonance of the optic’s suspension system, while the peak at 3 Hz is due to the resonance of the vibration isolation stack which supports the optical table in the vacuum chamber.

The dark gray “expected suppressed” trace is the “unsuppressed” convolved with the closed-loop transfer function from the common cavity displacement input to the residual displacement. This represents the expected contribution of seismic noise to the residual displacement once the arm length servo loop is closed. Since this motion is common to both laser frequencies its contribution is suppressed by the servo to an expected level of $\sim 10^{-12}$ m/ $\sqrt{\text{Hz}}$ across most of the band. However, it is nonetheless found to be one of the main contributors to the resultant arm displacement around 10 Hz.

2. Suspension thermal noise

The cylindrical cavity mirrors are suspended from a single wire loop clamped at the top of a suspension cage. The length of the pendulum is 25 cm, which leads to a fundamental pendulum frequency of $f_p = 1.0$ Hz. Suspension thermal noise originates from thermal fluctuation of these suspension wires. The noise is well modeled [26] and its power spectrum is expressed as

$$S_{\text{sus}}(f) = \frac{4k_B T}{(2\pi f)^2} \Re[Y(f)], \quad (7)$$

where k_B is the Boltzmann constant, T is the mean temperature, and f is the frequency. Y is the admittance of the suspended mirror due to an external force and is described by the transfer function

$$Y(f) = \frac{1}{M} \frac{if/(2\pi f_p^2)}{1 + i\phi_p - (f/f_p)^2}, \quad (8)$$

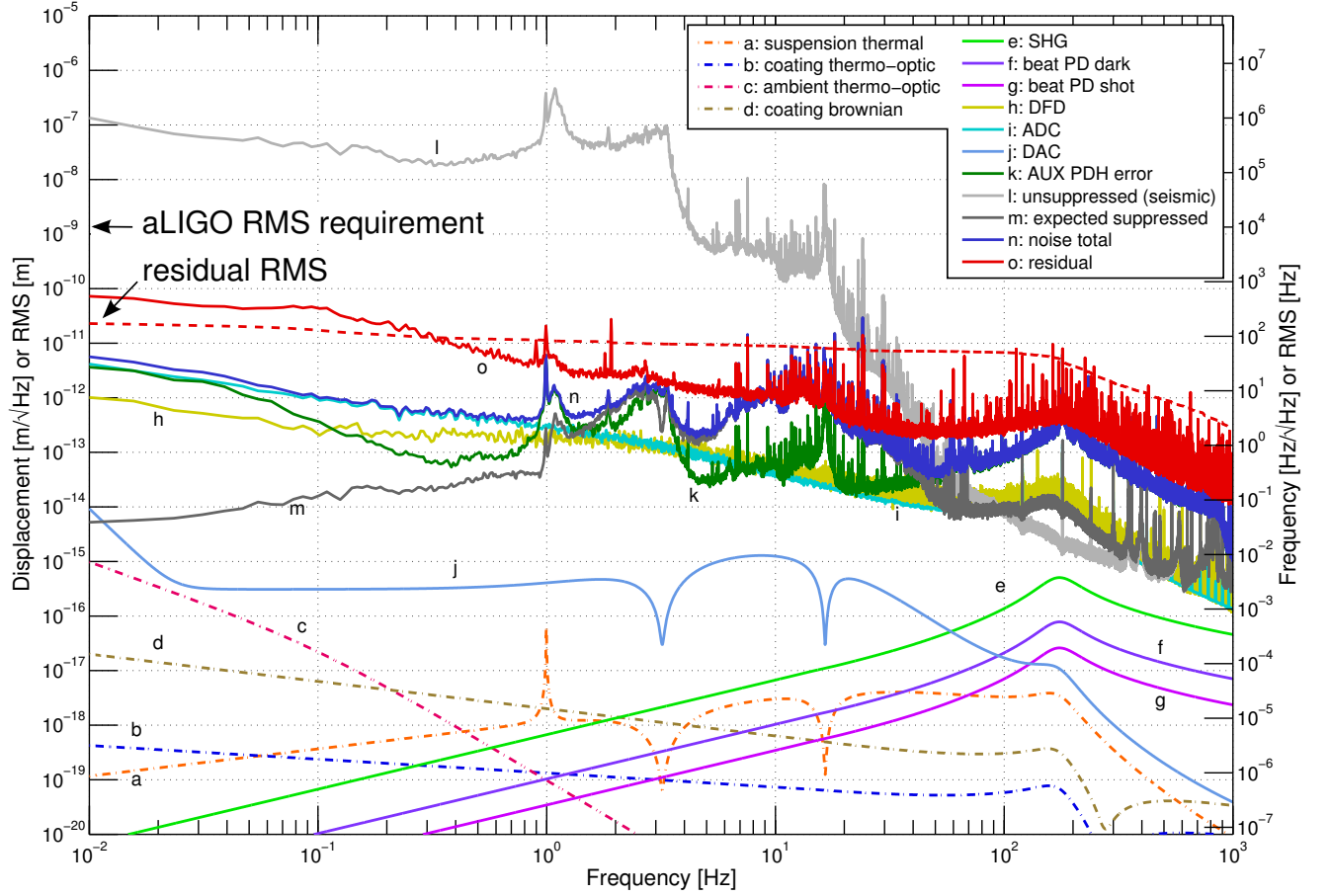


Fig. 7. Residual displacement noise at 1064 nm, and noise budget of the locked cavity. The right vertical axis indicates the corresponding frequency noise at 1064 nm. The solid red curve is the overall residual cavity displacement measured by the out-of-loop PSL PDH detector, while the red dashed curve is the residual displacement RMS integrated from high frequency. The colored dash-dot curves represent the estimated noise contributions from various fundamental noise sources, while the solid colored curves are the measured or estimated levels of the various technical noise sources.

where M is the pendulum mass, f_p is the pendulum frequency, and ϕ_p is the pendulum loss angle. As with seismic noise, this noise is common to both AUX and PSL beams so its contribution is suppressed by the arm length servo.

The expected suspension thermal noise level in our experiment is shown as the dot-dashed orange curve in Figure 7. The peak at 1 Hz is excess noise due to the pendulum resonance. The dip at 3.2 Hz is due to a resonant gain in the arm length servo used to suppress the contribution from the primary mode of the vibration isolation stack, while the dip at 16.5 Hz is resonant gain used to suppress the contribution from the bounce mode of the optic suspension.

3. Coating thermal noise

Noises associated with thermal fluctuations in the mirror's high-reflectivity coatings are an important limiting noise source in LIGO. While they are not expected to be a notable contribution to our result, we touch on them here for completeness.

There are two important coating thermal noise sources: *Brownian* noise comes from thermal vibrations associated with mechanical losses in the mirror coating. The combined *Thermo-refractive* and *thermo-elastic* noises, jointly referred to as *thermo-optic* (TO) noise, affects the laser field as it interacts with the high-reflective coating.

Unfortunately, calculating the effect of these noises in the presence multiple light wavelengths is not trivial. As mentioned in section 3 E, only the noises sensed differentially between the AUX and PSL beams, and therefore not suppressed by the arm length servo, will show up as residual displacement noise in our experiment. Calculating the differential effect accurately would therefore require a fully coherent analysis at both wavelengths, which we will not attempt here. Instead we make the very naive assumption that the difference between what is sensed by the AUX and PSL beams is entirely attributable to the difference in their spot sizes on the mirror surfaces. We then calculate the differential thermal noise contributions based on this differential spot area.

The Brownian thermal noise spectrum is given by [27]:

$$S_{\text{BR}}(f) = \frac{4k_B T}{2\pi f} \frac{\phi_{\text{eff}} (1 - P^2)}{E\sqrt{a}}, \quad (9)$$

where P is the Poisson ratio of the substrate, ϕ_{eff} is the effective loss angle of the coating, E is the Young's modulus of the substrate, and a is the area probed. The resultant residual displacement spectrum from coating Brownian noise in our experiment is shown as the dot-dashed brown curve in Figure 7.

For the thermo-optic (TO) noise contribution, we follow the coherent treatment proposed in [23]. A Gaussian beam illuminating a mirror senses thermal fluctuations in the coating resulting in the noise power spectrum:

$$S_{\text{TO}}^{\Delta T}(f) = 2\sqrt{2} \frac{k_B T^2}{a\sqrt{2\pi f \kappa s}}, \quad (10)$$

where κ is the thermal conductivity, and s is the heat capacity per volume. The overall thermo-optic noise spectrum is then

$$S_{\text{TO}}(f) = S_{\text{TO}}^{\Delta T}(f) \Gamma_{\text{tc}} (\chi_{\text{fsm}} \Delta \bar{\alpha} d - \bar{\beta} \lambda)^2, \quad (11)$$

where Γ_{tc} is a correction due to the finite thickness of the coating layers, $\Delta \bar{\alpha}$ is the difference in effective thermal expansion coefficient between the coating and substrate, χ_{fsm} is a correction due to the finite mirror size, d is the thickness of the layers, $\bar{\beta}$ is the effective thermo refractive coefficient, and λ is the beam wavelength. The residual displacement from thermo-optic noise is shown as the lower dot-dashed blue trace in Figure 7.

4. Couplings with ambient temperature fluctuations

Potentially more significant than the inherent thermo optic noise contribution at low frequencies is the thermo optic contribution from low frequency ambient temperature fluctuations coupling directly to the mirror coating. Thermal fluctuations in the mirror coating due to ambient temperature fluctuations in the lab can be significantly higher than those from thermo optic excitations. These fluctuations dominate the thermo optic noise spectrum at low frequencies.

To estimate the thermo optic noise contribution from ambient temperature we start with the same thermo optic noise description in equation 11. But instead of using the thermo optic fluctuations from equation 10, $S_{\text{TO}}^{\Delta T}$, we instead use an estimated thermal spectrum given by:

$$S_{\delta T}^{\Delta T}(f) = [\delta T(f) C(f) j(f)]^2, \quad (12)$$

where $\delta T(f)$ is the amplitude spectrum of the ambient temperature fluctuations in the lab environment,

$$\delta T(f) = 3 \times 10^{-3} \left(\frac{0.01 \text{ Hz}}{f} \right) \frac{\text{K}}{\sqrt{\text{Hz}}}, \quad (13)$$

$C(f)$ is the transfer function through the vacuum envelope, described by a single 0f.1 Hz pole, and $j(f)$ is the

radiative transfer to the optic surface,

$$j(f) = \frac{4\epsilon\sigma T^3}{2\pi\sqrt{f\kappa\rho c}}, \quad (14)$$

where ϵ is the emissivity of the coating, σ is the Stefan-Boltzmann constant, T is the mean temperature, κ is the thermal conductivity of the substrate, ρ is the density of the substrate, and c is the specific heat capacity. The contribution from this affect is shown as the pink dot-dashed curve in Figure 7.

B. Technical noise sources

This section describes the contribution from various technical noise sources that can be measured directly in the experiment.

1. Laser frequency noise

Frequency noise associated with the AUX and PSL lasers is generally suppressed by the control loops that keep the lasers locked to the main arm and mode cleaner cavities. However, since all control loops are coupled together at some level, there is a possibility of laser frequency noise contributing to the measured residual displacement noise.

As discussed in section 3B frequency noise from the PSL is significantly suppressed and can therefore be ignored. However, coupling from the AUX laser is at a much higher level. We estimate its contribution by observing the residual noise in the AUX PDH error signal while the AUX-cavity loop is locked. We then assume that this noise is due almost entirely to unsuppressed laser frequency noise fluctuations. The resultant contribution from this noise is the dark green ‘‘AUX PDH error’’ trace in Figure 7.

2. Second-harmonic generation noise

Noise due to the second-harmonic generation process is assumed to be added to the frequency noise of the frequency-doubled laser beam. The upper limit of the noise level is assumed to be $1 \times 10^{-5} f \text{ Hz}/\sqrt{\text{Hz}}$ [28]. Laser frequency doubling happens in two places in our experiment: in the AUX laser output and on the PSL beam for the beat note detection. The contribution from the PSL doubling in the beat note detection is much more significant, so it is this level that is shown as the light green curve in Figure 7.

3. Shot noise and detector dark noise

Both shot noise and dark noise appear as white noise (in the detection band) in the broadband RF photodetectors used in the experiment. When measuring the frequency of a signal, the measured voltage noise can be converted to frequency noise on the detected signal by [29]:

$$S_{\text{PD}}(f) = \frac{2S_V(f)}{V_{\text{RF}}^2} f^2, \quad (15)$$

where S_V is the input-referred voltage noise, and V_{RF} is the voltage amplitude of the main RF signal.

The most dominant contribution from these noises comes from the beat note detection photodetector. The dark current noise level of the photodetector used is $12 \text{ pA}/\sqrt{\text{Hz}}$ between 10 MHz and 80 MHz. The incident power on the PD is $200 \text{ } \mu\text{W}$ which produces $60 \text{ } \mu\text{A}$ of DC photocurrent, corresponding to a shot noise level of $4 \text{ pA}/\sqrt{\text{Hz}}$. The resultant frequency noise spectra at the detector input for these noise sources are shown as the purple (dark) and magenta (shot) traces in Figure 7.

4. Frequency discriminator noise

The comparator in the delay-line frequency discriminator adds white noise during the process of reshaping RF signals into square waves. The noise level is measured from the output of the DFD while being driven by a pure RF sine wave. The level, referred to the input of the DFD, was found to have a total contribution of $10^{-14} - 10^{-13} \text{ m}/\sqrt{\text{Hz}}$ after applying the loop correction factor (olive curve in Figure 7).

5. ADC noise

ADC noise is easily measured directly by terminating the inputs to the analog filters that whiten the signal before digitization, and then measuring the spectrum digitally. The affect of the of the ADC whitening is compensated for within the digital system. The resultant contribution, referred to the input of the DFD, sees the same loop correction factor as the DFD (cyan trace in Figure 7).

6. DAC noise

DAC noise is directly measured by digitally generating a 3 Hz signal, representing the peak frequency of the error signal while locked, and then measuring the output noise spectrum. The resultant noise contribution is mostly flat at a level of about $1 \text{ } \mu\text{V}/\sqrt{\text{Hz}}$ and is shown as the pale blue curve in Figure 7). The dips at 3.2 Hz and 16.5 Hz are due to the affect of the resonant gains stages discussed in section 4A 2.

C. Scaling noise sources for Advanced LIGO

In this section we look briefly at how various noise sources in our experiment can be scaled to Advanced LIGO. We find that certain noise contributions will be more prominent in aLIGO, but that they are addressed in the aLIGO design such that they should not pose a significant problem.

1. Frequency noise

From the relation between frequency noise and length fluctuations expressed in equation 2 we can see that the 100-times longer arm cavities of aLIGO means that aLIGO will be 100 times more sensitive to laser frequency fluctuations. For a displacement noise requirement of 1 nm RMS, the beat note frequency stability requirement goes from 8.8 kHz in the 40m experiment to 83 Hz in aLIGO. This puts a much stricter requirement on the frequency noise of the AUX laser and SHG noises.

Advanced LIGO will mitigate this issue in a couple of different ways. First, aLIGO will phase lock the AUX

laser to the PSL frequency through the use of a fiber-based phase-locked loop (PLL). This will improve noise below 50 Hz, while making it worse at high frequencies. The increased high frequency noise can then be addressed through optimization of the servo controls. The gain of the AUX-cavity loop can be increased to suppress the excess noise from the AUX laser, and the bandwidth of the arm length stabilization loop can be decreased so that any residual noise will not be injected into the cavity motion.

2. Readout and frequency discriminator noise

Readout and electronics noise sources should become less severe in aLIGO. The interferometer response will generally grow in proportion to length, resulting in a higher SNR against these noise sources.

The frequency discriminator, on the other hand, generally does not scale with the base line length since it reads out the frequency of the beat note rather than the optical phase. For this reason the readout noise of the discriminator will make a 100 times larger contribution to the noise budget than it does in our experiment. This could likely be the limiting noise source with a frequency noise level of $1 \text{ Hz}/\sqrt{\text{Hz}}$ at 10 Hz. The situation can be improved by using a small-range discriminator such as a VCO-based PLL or a longer cable in the DFD.

3. Seismic length fluctuations

Length fluctuations due to seismic noise should become somewhat easier to handle in aLIGO since the test masses will be far more isolated from ground vibration due to sophisticated aLIGO seismic isolation systems. Depending on how large the residual seismic fluctuations are the unity gain frequency of the arm length servo loop should be able to be lowered. This is generally good since it avoids injection of undesired control noises at high frequencies.

5. Future Work

Besides precise control of suspended Fabry-Perot cavities, multi-wavelength readout also has the potential to improve performance of other optical systems. Here we present futuristic ideas which can potentially reduce the fundamental noise sources such as quantum noise and mirror thermal noise through the use of multi-wavelength readout, as well as an idea to precisely characterize an optical cavity.

A. Multi-wavelength readout for manipulating the quantum noise limit

By resonating multiple laser beams with different wavelengths in a single interferometer, traditional quantum noise limits can potentially be modified.

One example is cancellation of quantum back-action for GW detectors [30]. Imagine a main carrier field resonating with high power in an interferometer arm cavity, and a low-power auxiliary laser beam with a different wavelength resonant only in the interferometer vertex

(anti-resonant in the arm cavities). The high-power main carrier field would produce quantum radiation pressure noise on the test masses. The low-power auxiliary laser beam, on the other hand, would sense only the differential motion of the two input test masses, and therefore not be sensitive to gravitational wave signals. An optimal combination of the two carriers beam with Wiener filters could then be used to cancel the low-frequency back action noise, while not losing information from gravitational waves.

Another idea is to resonate both carrier wavelengths in the arm cavities. The design of the optics could be made such that the optical properties for the different wavelengths are different leading to different frequency sensitivities for the two beams. For example, the input test masses could have higher transmittance for one wavelength over the other. By tuning different wavelengths and optimally combining their outputs, one may be able to shape the quantum noise spectrum in a much more flexible way than in the single wavelength case.

Multiple beams with different wavelengths could also potentially be used to manipulate the dynamics of test masses in optical cavities. In particular, it is well known that the multi-bounce laser fields in optical cavities modify the dynamics of the cavity mirrors via radiation pressure [31]. Under appropriate conditions this can result in modifications of the opto-mechanical coupling and a higher response against optical phase changes. For example, in gravitational wave detectors that use signal-recycling cavities, two wavelengths of light appropriately detuned from the resonance of the signal-recycling cavity can result in a radiation pressure force that reduces the effective inertia of the test mass at low frequencies. This can significantly amplify the response of the interferometer to gravitational-wave signals [32]. It is therefore possible that a multi-wavelength technique could allow for surpassing the standard quantum limit over a broad frequency band.

B. Thermal noise estimation

In a frequency regime where sensitivity is strongly limited by mirror thermal noise, it may be possible to use two different laser wavelengths to differentially sense the thermal noise in the two fields. It may then be possible to combine signals from the two lasers in order to yield one data stream representing the cavity length fluctuations and another with purely the thermal noise. This technique may be capable of giving a moderate decrease in the effective thermal noise. However, the differential frequency noise between the wavelengths would need to be investigated more precisely.

C. Precise cavity mode characterization

Since multi-wavelength metrology enables us to detune the laser frequency from one of the cavity resonances in a quasi-static manner, various longitudinal and spacial characteristics of the cavity can be precisely inspected.

Precise scanning of a resonance can provide a measure of cavity finesse, while scanning over multiple free spectral ranges gives us a measurement of the absolute length of the cavity. The frequency spacing of transverse spatial modes can be obtained by inspecting the resonances of the fundamental and higher-order modes, therefore providing information about the cavity geometry and the figure error of the cavity optics. The power transmitted during scanning can also tell us the mode matching efficiency between an incident beam and cavity eigenmodes.

6. Conclusions

Using multiple lasers, we have demonstrated a tractable strategy for sensing the cavity lengths of a complex interferometer for gravitational wave detection. This method can be replicated and applied to any of the detectors in the upcoming worldwide network (LIGO, Virgo, KAGRA).

The noise limits are now well understood and well below the requirements necessary for aLIGO. The mirror masses for these new detectors are 30-40 kg and they have thermal time constants of several hours. Long periods spent without the interferometer locked introduce enormous thermal transients in the interferometer which perturb the delicate operating state. The use of this technique should allow for a significantly higher duty cycle in the future.

In addition, the technique has promise to improve the sensitivity of the next generation of interferometers through the use of multi-wavelength readout to partially cancel some of the thermal and quantum noises which limit the more conventional designs.

Appendix A: Control Model Transfer Functions

Table 2 lists all of the zeros, poles, and gains for the various control elements in the control model described in section 3 and Figure 5. For a system with p_m poles and z_n zeros (both specified in Hz) and gain k , the transfer function would be given by:

$$X(f) = k \frac{\prod_n (1 + if/z_n)}{\prod_m (1 + if/p_m)}, \quad (\text{A1})$$

Figure 8 shows Bode plots (amplitude and phase) of a couple of the key transfer functions from the full control model.

In addition to the blocks represented in Table 2, the blocks labeled “ $L \rightarrow \nu$ ” in Figure 5 represent the conversion from displacement (dL) to frequency ($d\nu$) described in equation 2, i.e.:

$$L \rightarrow \nu = \frac{\nu}{L}, \quad (\text{A2})$$

where $\nu = c/\lambda$.

element	zeros (Hz)	poles (Hz)	gain
C_{AUX}	-	18.5k	1
D_{AUX}	-	-	5.0e-6
F_{AUX}	1.0, 100, 10k	0.1m, 1.2, 2.0	2.1e8
A_{AUX}	-	100k	5.0e6
D_{DFD}	-	-	2.16e-7
	40, 40,	1.0m, 500,	
F_{ALS}	$1.655 \pm 2.739i$, $3.320 \pm 16.163i$	$0.052 \pm 3.200i$, $0.105 \pm 16.500i$	1.0e6
A_{TM}	-	$0.1 \pm 0.995i$	8.0e7
C_{PSL}	-	3.8k	1
D_{PSL}	-	-	2.5e-5
F_{PSL}	4k, 20k, 20k	40, 1k, 1k	2.3e4
A_{PSL}	-	100k	5.0e6
SHG	-	-	2

Table 2. Zeros, poles and gain of the control model blocks.

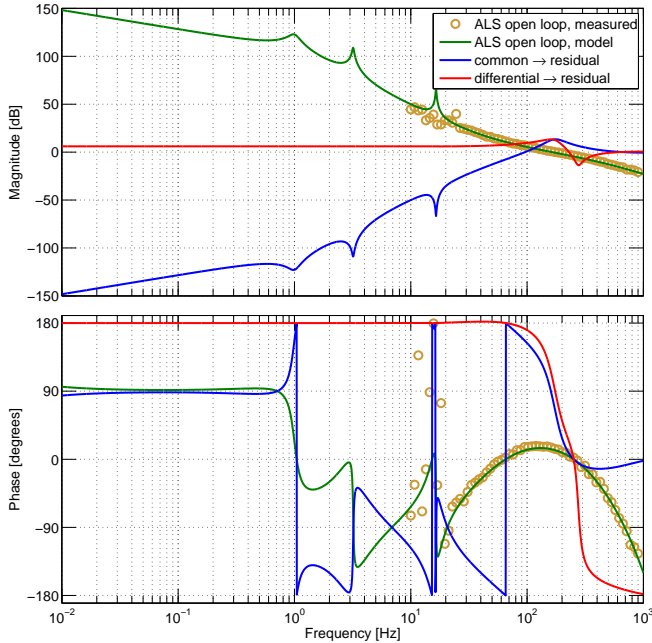


Fig. 8. Bode plot of control model transfer functions. The green trace is the full open-loop transfer function of the arm length servo control loop. The blue and red traces are the transfer functions from external disturbances to residual displacement, for AUX/PSL common and differential sensing.

Appendix B: Symbol Definitions and Values

Table 3 shows the values used for various variables in the text, including all fundamental constants, experimental values, and material properties.

symbol	name	value	SI unit
k_B	Boltzmann's constant	1.38e-23	J K ⁻¹
σ	Stefan-Boltzmann constant	5.67e-8	W m ⁻² K ⁻⁴
T	mean temperature	290	K
λ	beam wavelength	1.064e-6	m
M	cavity mirror pendulum mass	0.243	kg
f_p	pendulum frequency	1.0	Hz
ϕ_p	pendulum loss angle	1.7e-4	-
P	Poisson ratio of (substrate)	0.167	-
E	Young's modulus (substrate)	7.27e10	N m ⁻¹
κ	thermal conductivity	1.38	W m ⁻¹ K ⁻¹
s	heat capacity per volume	1.62e6	m ⁻³ K ⁻¹
c	specific heat capacity	740	J kg ⁻¹ K ⁻¹
ϵ	emissivity	0.9	-
ρ	density	2202	kg m ⁻³
ITM			
ϕ_{eff}	effective coating loss angle	8.65e-8	-
$\Delta\bar{\alpha}$	effective thermal expansion difference	3.59e-6	K ⁻¹
$\bar{\beta}$	effective thermal refraction	2.35e-6	K ⁻¹
ETM			
ϕ_{eff}	effective coating loss angle	1.24e-7	-
$\Delta\bar{\alpha}$	effective thermal expansion difference	4.54e-6	K ⁻¹
$\bar{\beta}$	effective thermal refraction	1.11e-6	K ⁻¹

Table 3. Values of fundamental constants, and material properties and variables for the 40m mirror coatings. If not specified, material properties are for the mirror coating.

Acknowledgments

We gratefully acknowledge illuminating discussions with Bram Slagmolen, Nicolas Smith-Lefebvre and Peter Fritschel. We also thank the National Science Foundation for support under grant PHY-0555406.

References

1. A. Abramovici, W. E. Althouse, R. W. P. Drever, Y. Gürsel, S. Kawamura, F. J. Raab, D. Shoemaker, L. Sievers, R. E. Spero, K. S. Thorne, R. E. Vogt, R. Weiss, S. E. Whitcomb, and M. E. Zucker, “LIGO: The laser interferometer gravitational-wave observatory,” *Science* **256**, 325–333 (1992).
2. B. Abbott, R. Abbott, R. Adhikari, P. Ajith, B. Allen, G. Allen, R. Amin, S. Anderson, W. Anderson, M. Arain *et al.*, “LIGO: the laser interferometer gravitational-wave observatory,” *Reports on Progress in Physics* **72**, 076901 (2009).

3. T. Accadia, F. Acernese, F. Antonucci, P. Astone, G. Ballardín, F. Barone, M. Barsuglia, A. Basti, T. S. Bauer, M. Bebronne, M. G. Beker, A. Belletoile, S. Birindelli, M. Bitossi, M. A. Bizouard, M. Blom, F. Bondu, L. Bonelli, R. Bonnard, V. Boschi, L. Bosi, B. Bouhou, S. Braccini, C. Bradaschia, M. Branchesi, T. Briant, A. Brillet, V. Brisson, R. Budzyński, T. Bulik, H. J. Bulten, D. Buskulic, C. Buy, G. Cagnoli, E. Calloni, B. Canuel, F. Carbognani, F. Cavalier, R. Cavalieri, G. Cella, E. Cesarini, O. Chaibi, E. C. Mottin, A. Chincarini, F. Cleva, E. Coccia, P.-F. Cohadon, C. N. Colacino, J. Colas, A. Colla, M. Colombini, A. Corsi, J.-P. Coulon, E. Cuoco, S. D'Antonio, V. Dattilo, M. Davier, R. Day, R. D. Rosa, G. Debreczeni, W. D. Pozzo, M. del Prete, L. D. Fiore, A. D. Lieto, M. D. P. Emilio, A. D. Virgilio, A. Dietz, M. Drago, V. Fafone, I. Ferrante, F. Fidecaro, I. Fiori, R. Flaminio, L. A. Forte, J.-D. Fournier, J. Franc, S. Frasca, F. Frasconi, M. Galimberti, L. Gammaitoni, F. Garuffi, M. E. Gáspár, G. Gemme, E. Genin, A. Gennai, A. Giazotto, R. Gouaty, M. Granata, C. Greverie, G. M. Guidi, J.-F. Hayau, A. Heidmann, H. Heitmann, P. Hello, D. Huet, P. Jaranowski, I. Kowalska, A. Królak, N. Leroy, N. Letendre, T. G. F. Li, N. Liguori, M. Lorenzini, V. Lorette, G. Losurdo, E. Majorana, I. Maksimovic, N. Man, M. Mantovani, F. Marchesoni, F. Marion, J. Marque, F. Martelli, A. Masserot, C. Michel, L. Milano, Y. Minenkov, M. Mohan, N. Morgado, A. Morgia, S. Mosca, V. Moscatelli, B. Mours, F. Nocera, G. Pagliaroli, L. Palladino, C. Palomba, F. Paoletti, M. Parisi, A. Pasqualetti, R. Passaquieti, D. Passuello, G. Persichetti, M. Pichot, F. Piergiovanni, M. Pietka, L. Pinard, R. Poggiani, M. Prato, G. A. Prodi, M. Punturo, P. Puppo, D. S. Rabeling, I. Rácz, P. Rapagnani, V. Re, T. Regimbau, F. Ricci, F. Robinet, A. Rocchi, L. Rolland, R. Romano, D. Rosińska, P. Ruggi, B. Sassolas, D. Sentenac, L. Sperandio, R. Sturani, B. Swinkels, M. Tacca, L. Taffarello, A. Toncelli, M. Tonelli, O. Torre, E. Tournefier, F. Travasso, G. Vajente, J. F. J. van den Brand, C. V. D. Broeck, S. van der Putten, M. Vasuth, M. Vavoulidis, G. Vedovato, D. Verkindt, F. Vetrano, A. Viceré, J.-Y. Vinet, S. Vitale, H. Vocca, R. L. Ward, M. Was, M. Yvert, and J.-P. Zendri, "Status of the Virgo project," *Classical and Quantum Gravity* **28**, 114002 (2011).
4. H. Grote (for the LIGO Scientific Collaboration), "The status of GEO 600," *Classical and Quantum Gravity* **25**, 114043 (2008).
5. K. Kuroda and the LCGT Collaboration, "Status of LCGT," *Classical and Quantum Gravity* **27**, 084004 (2010).
6. G. M. Harry and the LIGO Scientific Collaboration, "Advanced LIGO: the next generation of gravitational wave detectors," *Classical and Quantum Gravity* **27**, 084006 (2010).
7. K. A. Strain and B. N. Shapiro, "Damping and local control of mirror suspensions for laser interferometric gravitational wave detectors," *Review of Scientific Instruments* **83**, 044501 (2012).
8. J. Camp, L. Sievers, R. Bork, and J. Heefner, "Guided lock acquisition in a suspended fabry-perot cavity," *Opt. Lett.* **20**, 2463–2465 (1995).
9. M. Evans, N. Mavalvala, P. Fritschel, R. Bork, B. Bhawal, R. Gustafson, W. Kells, M. Landry, D. Sigg, R. Weiss, S. Whitcomb, and H. Yamamoto, "Lock acquisition of a gravitational-wave interferometer," *Opt. Lett.* **27**, 598–600 (2002).
10. F. Acernese, M. Alshourbagy, P. Amico, F. Antonucci, S. Aoudia, K. Arun, P. Astone, S. Avino, L. Baggio, G. Ballardín, F. Barone, L. Barsotti, M. Barsuglia, T. Bauer, S. Bigotta, S. Birindelli, M. Bizouard, C. Boccara, F. Bondu, L. Bosi, S. Braccini, C. Bradaschia, A. Brillet, V. Brisson, D. Buskulic, G. Cagnoli, E. Calloni, E. Campagna, F. Carbognani, F. Cavalier, R. Cavalieri, G. Cella, E. Cesarini, E. Chassande-Mottin, S. Chatterji, F. Cleva, E. Coccia, C. Corda, A. Corsi, F. Cottoné, J.-P. Coulon, E. Cuoco, S. D'Antonio, A. Dari, V. Dattilo, M. Davier, R. D. Rosa, M. D. P. Prete, L. D. Fiore, A. D. Lieto, M. D. P. Emilio, A. D. Virgilio, M. Evans, V. Fafone, I. Ferrante, F. Fidecaro, I. Fiori, R. Flaminio, J.-D. Fournier, S. Frasca, F. Frasconi, L. Gammaitoni, F. Garuffi, E. Genin, A. Gennai, A. Giazotto, V. Granata, C. Greverie, D. Grosjean, G. Guidi, S. Hamdani, S. Hebri, H. Heitmann, P. Hello, D. Huet, S. Kreckelbergh, P. L. Penna, M. Laval, N. Leroy, N. Letendre, B. Lopez, M. Lorenzini, V. Lorette, G. Losurdo, J.-M. Mackowski, E. Majorana, C. Man, M. Mantovani, F. Marchesoni, F. Marion, J. Marque, A. Masserot, F. Menzinger, C. Michel, L. Milano, Y. Minenkov, S. Mitra, M. Mohan, J. Moreau, N. Morgado, S. Mosca, B. Mours, I. Neri, F. Nocera, G. Pagliaroli, C. Palomba, F. Paoletti, S. Pardi, A. Pasqualetti, R. Passaquieti, D. Passuello, F. Piergiovanni, L. Pinard, R. Poggiani, M. Punturo, P. Puppo, O. Rabaste, P. Rapagnani, T. Regimbau, F. Ricci, I. Ricciardi, A. Rocchi, L. Rolland, R. Romano, P. Ruggi, D. Sentenac, S. Solimeno, B. Swinkels, R. Terenzi, A. Toncelli, M. Tonelli, E. Tournefier, F. Travasso, G. Vajente, J. van den Brand, S. van der Putten, D. Verkindt, F. Vetrano, A. Viceré, J.-Y. Vinet, H. Vocca, and M. Yvert, "Lock acquisition of the Virgo gravitational wave detector," *Astroparticle Physics* **30**, 29 – 38 (2008).
11. A. J. Mullavey, B. J. J. Slagmolen, J. Miller, M. Evans, P. Fritschel, D. Sigg, S. J. Waldman, D. A. Shaddock, and D. E. McClelland, "Arm-length stabilisation for interferometric gravitational-wave detectors using frequency-doubled auxiliary lasers," *Opt. Express* **20**, 81–89 (2012).

12. D. A. Shaddock, "Digitally enhanced heterodyne interferometry," *Opt. Lett.* **32**, 3355–3357 (2007).
13. O. P. Lay, S. Dubovitsky, D. A. Shaddock, and B. Ware, "Coherent range-gated laser displacement metrology with compact optical head," *Opt. Lett.* **32**, 2933–2935 (2007).
14. Y. Aso, M. Ando, K. Kawabe, S. Otsuka, and K. Tsubono, "Stabilization of a Fabry-Pérot interferometer using a Suspension-Point Interferometer," *Phys. Lett. A* **327** (2004).
15. K. Numata and J. Camp, "Interferometric testbed for nanometer level stabilization of environmental motion over long time scales," *Appl. Opt.* **47**, 6832–6841 (2008).
16. O. Miyakawa, R. Ward, R. Adhikari, B. Abbott, R. Bork, D. Busby, M. Evans, H. Grote, J. Heefner, A. Ivanov, S. Kawamura, F. Kawazoe, S. Sakata, M. Smith, R. Taylor, M. Varvella, S. Vass, and A. Weinstein, "Lock acquisition scheme for the advanced ligo optical configuration," *Journal of Physics: Conference Series* **32**, 265 (2006).
17. O. Miyakawa, R. Ward, R. Adhikari, M. Evans, B. Abbott, R. Bork, D. Busby, J. Heefner, A. Ivanov, M. Smith, R. Taylor, S. Vass, A. Weinstein, M. Varvella, S. Kawamura, F. Kawazoe, S. Sakata, and C. Mow-Lowry, "Measurement of optical response of a detuned resonant sideband extraction gravitational wave detector," *Phys. Rev. D* **74**, 022001 (2006).
18. R. L. Ward, R. Adhikari, B. Abbott, R. Abbott, D. Barron, R. Bork, T. Fricke, V. Frolov, J. Heefner, A. Ivanov, O. Miyakawa, K. McKenzie, B. Slagmolen, M. Smith, R. Taylor, S. Vass, S. Waldman, and A. Weinstein, "DC readout experiment at the Caltech 40m prototype interferometer," *Classical and Quantum Gravity* **25**, 114030 (2008).
19. B. J. Meers, "Recycling in laser-interferometric gravitational-wave detectors," *Phys. Rev. D* **38**, 2317 (1988).
20. J. Mizuno, K. Strain, P. Nelson, J. Chen, R. Schilling, A. Rüdiger, W. Winkler, and K. Danzmann, "Resonant sideband extraction: a new configuration for interferometric gravitational wave detectors," *Physics Letters A* **175**, 273 – 276 (1993).
21. R. W. P. Drever, J. L. Hall, F. V. Kowalski, J. Hough, G. M. Ford, A. J. Munley and H. Ward, "Laser phase and frequency stabilization using an optical resonator," *Appl. Phys. B* **31**, 97 (1983).
22. S. Greenstein and M. Rosenbluh, "Dynamics of cw intra-cavity second harmonic generation by PPKTP," *Optics Communications* **238**, 319 – 327 (2004).
23. M. Evans, S. Ballmer, M. Fejer, P. Fritschel, G. Harry, and G. Ogin, "Thermo-optic noise in coated mirrors for high-precision optical measurements," *Phys. Rev. D* **78**, 102003 (2008).
24. S. Schilt, N. Bucalovic, L. Tombez, V. Dolgovskiy, C. Schori, G. D. Domenico, M. Zaffalon, and P. Thomann, "Frequency discriminators for the characterization of narrow-spectrum heterodyne beat signals: Application to the measurement of a sub-hertz carrier-envelope-offset beat in an optical frequency comb," *Review of Scientific Instruments* **82**, 123116 (2011).
25. P. Fritschel, D. McClelland, A. Mullavey, D. Shaddock, B. Slagmolen, and S. Waldman, "Advanced LIGO arm length stabilisation requirements," *LIGO DCC LIGO-T0900095-v2* (2009).
26. G. Gonzalez, "Suspensions thermal noise in the LIGO gravitational wave detector," *Classical and Quantum Gravity* **17**, 4409 (2000).
27. G. M. Harry, M. R. Abernathy, A. E. Becerra-Toledo, H. Armandula, E. Black, K. Dooley, M. Eichenfield, C. Nwabugwu, A. Villar, D. R. M. Crooks, G. Cagnoli, J. Hough, C. R. How, I. MacLaren, P. Murray, S. Reid, S. Rowan, P. H. Sneddon, M. M. Fejer, R. Route, S. D. Penn, P. Ganau, J.-M. Mackowski, C. Michel, L. Pinard, and A. Remillieux, "Titania-doped tantala/silica coatings for gravitational-wave detection," *Classical and Quantum Gravity* **24**, 405 (2007).
28. D. Yeaton-Massey and R. Adhikari, "A new bound on excess frequency noise in second harmonic generation in PPKTP at the 10^{-19} level," in preparation (2012).
29. D. H. Wolaver, *Phase-Locked Loop Circuit Design* (PTR Prentice Hall, 1991).
30. H. Rehbein, H. Müller-Ebhardt, K. Somiya, C. Li, R. Schnabel, K. Danzmann, and Y. Chen, "Local readout enhancement for detuned signal-recycling interferometers," *Phys. Rev. D* **76**, 062002 (2007).
31. A. Buonanno and Y. Chen, "Signal recycled laser-interferometer gravitational-wave detectors as optical springs," *Phys. Rev. D* **65**, 042001 (2002).
32. F. Khalili, S. Danilishin, H. Müller-Ebhardt, H. Miao, Y. Chen, and C. Zhao, "Negative optical inertia for enhancing the sensitivity of future gravitational-wave detectors," *Phys. Rev. D* **83**, 062003 (2011).